



## Notes on the photo-induced characteristics of transition metal-doped and undoped titanium dioxide thin films

S. Kment<sup>a,b,\*</sup>, H. Kmentova<sup>c</sup>, P. Kluson<sup>c</sup>, J. Krysa<sup>b</sup>, Z. Hubicka<sup>a</sup>, V. Cirkva<sup>c</sup>, I. Gregora<sup>a</sup>, O. Solcova<sup>c</sup>, L. Jastrabik<sup>a</sup>

<sup>a</sup> Institute of Physics, Academy of Sciences of the Czech Republic, Na Slovance 2, 182 21 Prague 8, Czech Republic

<sup>b</sup> Institute of Chemical Technology, ICT Prague, Technicka 5, 166 28 Prague 6, Czech Republic

<sup>c</sup> Institute of Chemical Process Fundamentals, Academy of Sciences of the Czech Republic, Rozvojova 135, 165 02 Prague 6, Czech Republic

### ARTICLE INFO

#### Article history:

Received 22 January 2010

Accepted 1 April 2010

Available online 8 April 2010

#### Keywords:

Sol–gel

Thin layers

Metal-doped TiO<sub>2</sub>

IPCE

Photocurrent

Photocatalysis

### ABSTRACT

This study reports the preparation of thin nanoparticulate films of titanium dioxide and its modified version doped with a transition metal. The behavior of prepared films was described by means of their photocatalytic and photo-induced electrochemical properties. The TiO<sub>2</sub> and M/TiO<sub>2</sub> (M = Ag, Zr, Fe) thin films were produced via a standard sol–gel method using titanium *n*-butoxide, acetylacetone, and transition metal acetylacetonates as precursors. Prepared films were analyzed by a series of techniques involving XRD, Raman spectroscopy, SEM, AFM, and XPS. Their photocatalytic activity was monitored with the aid of decomposition of the model compound Rhodamine B in water. All films were then tested for their photo-induced electrochemical properties based on evaluation of polarization curves (photocurrents). The highest reaction rate constant (0.0101 min<sup>-1</sup>), which was even higher than that for pure TiO<sub>2</sub>, was obtained for the Ag/TiO<sub>2</sub> sample. The highest quantum yield of the charge collection was determined for the undoped TiO<sub>2</sub> film.

© 2010 Elsevier Inc. All rights reserved.

### 1. Introduction

Titanium dioxide (TiO<sub>2</sub>) has been of great interest because of its wide range of industrial applications. TiO<sub>2</sub> has also received a great deal of attention due to its chemical stability, nontoxicity, low cost, etc. It has been reported in processes for photodegradation of various compounds [1–8], as a part of gas sensors [9], solar cells [10], antifogging coatings [11], and numerous thin-film optical devices [12]. Thin films of titanium dioxide have been prepared, among others, by chemical methods such as the hydrothermal technique [13,14], chemical vapor deposition (CVD) [15,16], or the sol–gel route. The sol–gel method is one of the more successful techniques for preparing nanosized metallic oxides, often revealing enhanced photocatalytic activity [17,18]. The sol–gel-derived precipitates are amorphous in nature, requiring further heat treatment at high temperatures to induce the inevitable crystallization [19–22]. Photoactivity of crystal TiO<sub>2</sub> arises from the photo-generated electrons and holes. These charge carriers either recombine inside the particle or move to its surface where they can react with adsorbed molecules. Positive holes typically oxidize organic compounds, while electrons mainly reduce molecular oxygen to superoxide

radical anions [23–25]. However, most of the photo-induced positive holes and electrons recombine. If the recombination occurs quickly (lifetime of charge carriers is about 30 ns) there is not enough time for other chemical reactions [26,27]. Many attempts have been made to dope the titanium dioxide with transition metals such as iron [28], cobalt [29], nickel [30], manganese [31], chromium [32], vanadium [33], copper [34], molybdenum [35], wolfram [36], zinc [37], zirconium [38,39], and silver [40,41]. Such metal creates a “new” electron states inside the TiO<sub>2</sub> forbidden band, which can capture the excited electrons from the TiO<sub>2</sub> valance band and thus preserve the holes [42]. It can also allow the light absorption to be widened into the visible region to various extents, depending on the type of the dopant and its concentration. Therefore the photocatalysis on TiO<sub>2</sub> can be promoted using visible light. The photodegradation of various substrates is then a complex function of the dopant, the concentration, and the microstructural characteristics of the catalyst. Usually there is a critical doping concentration at which any further increase results in the charge carrier recombination, thus lowering the photoactivity of the prepared samples [43]. It has been found, however, that doping of the TiO<sub>2</sub> crystals with transition metal ions reduces in some cases the photooxidation rates compared to pristine TiO<sub>2</sub> [44]. Another possibility of reducing the electron/hole pairs recombination is the application of an external voltage bias on a photoanode (here TiO<sub>2</sub> deposited onto a conductive support). Photo-generated

\* Corresponding author at: Institute of Physics, Academy of Sciences of the Czech Republic, Na Slovance 2, 182 21 Prague 8, Czech Republic. Fax: +420 286 581 448.  
E-mail address: kment@fzu.cz (S. Kment).

carriers are sufficiently separated due to the electrons' withdrawal toward the conducting back-contact (at which the potential is applied). Therefore the overall amount of the holes initiating the oxidation reactions at the TiO<sub>2</sub> surface is increased and thus the photocatalytic process is significantly enhanced [45–48].

The major objectives of the study are fundamental aspects of the sol–gel process for the formation of TiO<sub>2</sub> and TiO<sub>2</sub>-doped nanoparticulate thin films and their functional features in photochemical and photoelectrochemical events. For this purpose a series of pristine TiO<sub>2</sub> and TiO<sub>2</sub>-doped by Ag, Zr, and Fe were prepared and described. The main aim of this work was to discuss the differences between photoelectrochemical and photocatalytic behavior of the fabricated pure and doped TiO<sub>2</sub> thin layers.

## 2. Materials and methods

### 2.1. Chemicals

Titanium *n*-butoxide (97%), acetylacetone (99.5%), and ethyl alcohol (99%) were used as received (all from Sigma–Aldrich, Prague, CR) for the photocatalyst preparation. Zirconium (IV) acetylacetonate (98%), silver acetylacetonate (98%), and iron (III) acetylacetonate (Sigma–Aldrich) were used as obtained for the preparation of doped titania photocatalysts. Rhodamine B was used as received (Lachema, Brno, CR) for the photocatalytic experiments. All solutions were prepared using distilled water (conductivity 1 μS cm<sup>-1</sup>).

### 2.2. Preparation of TiO<sub>2</sub> and M/TiO<sub>2</sub> thin films

This section describes the sol–gel procedure employed in the preparation of the thin films [49]. The preparation might be divided into several consecutive steps—namely hydrolysis and condensation, gelling, aging, and thermal treatment (drying and calcination). Titanium *n*-butoxide, Ti(OBu)<sub>4</sub>, was used as the precursor. Titanium *n*-butoxide (10 ml) was dissolved in 10 ml of acetylacetone. Then 10 ml of ethanol containing 0.5 ml of hydrochloric acid was dropped slowly into the solution. Finally 4 ml of distilled water was added under vigorous stirring. For the doped TiO<sub>2</sub> the synthetic procedure followed the same routine but the appropriate amount (0.3 g) of metal acetylacetonate was dissolved in acetylacetone. Coatings on slides (microscopic slides and ITO–indium–tin oxide-coated substrates) were produced in a dip-coating machine with a withdrawal rate of 6 cm min<sup>-1</sup>. The films were then dried at room temperature for 1 h and calcined at 500 °C for 2 h (heating rate 2 °C/min).

### 2.3. Characterization of the prepared TiO<sub>2</sub> and M/TiO<sub>2</sub> thin films

Absorption edges were determined using absorption data of thin films recorded by a UV/Vis spectrophotometer (Shimadzu, UV-2450, Japan) in the range 200–800 nm. X-ray diffraction patterns were recorded on an XRD 7 diffractometer (Rich. Seifert & Co., Freiberg, Germany) to examine the crystallographic phase and it was also used for the estimation of the samples' crystallite size (Cu Kα radiation, ω = 1.5°, PB geometry, 2θ = 20–80°). Crystallographic structures of the samples were then examined by Raman spectroscopy (Renishaw Raman Microscope RM 1000) in a backscattering configuration. As the source of activation a 514 nm Ar<sup>+</sup> line at a power <1 mW, focused down to a spot of 2–3 μm in diameter, was used. X-ray photoelectron spectroscopy (XPS) was employed to examine both the valence state and the surface stoichiometries. To analyze the binding energies of the prepared samples, XPS spectra were recorded by an ESCA Probe P photoelectron spectrometer (Omicron Nanotechnology Ltd.,

Taunusstein, Germany) using the monochromatic Al Kα X-ray source with an energy of 1486.7 eV and pressure 10<sup>-10</sup> mbar. The measured spectra were analyzed with CasaXPS (Casa Software Ltd., Teignmouth, UK). The layers' morphologies and grain sizes were imaged using scanning electron microscopy (Hitachi S-4700, at 10 kV). Atomic force microscopy images were obtained using AFM Explorer (ThermoMicroscopes, Sunnyvale, CA, USA) and these were then analyzed to estimate the parameter of the relative surface roughness, etc.

### 2.4. Photo-induced electrochemical experiments

The general setup of the electrochemical test has been described previously [48]. Briefly, the electrochemical experiments were carried out in the system containing a three-chamber Pyrex electrochemical cell with a modified three-electrode arrangement. In this setup the titania-containing layer served as the working electrode and the Ag/AgCl (environment of 3 M KCl) as the reference one (potential of 207 mV vs. SHE). The platinum sheet was employed as the counterelectrode. The main part of the arrangement was positioned on an optical bench (Melles Griot, Albuquerque, NM, USA) with the electrochemical cell, a lamp (DC Arc polychromatic high-pressure mercury lamp Lot LSH201/2 Hg, Xe), filters, and a shade. All these parts were geometrically centered. A set of optical filters was employed as modifiers of the light beam in order to isolate the radiation wavelength (365 ± 10 nm). The size of the working electrode was limited to 1 cm<sup>2</sup> and a 0.1 M solution of Na<sub>2</sub>SO<sub>4</sub> was used as the electrolyte. The Voltalab PGZ-100 potentiostat (Radiometer Analytical SAS, Lyon, France) with operating software package Volta Master 4 (version 7) was used for the measurement of photocurrents. Incident-photon-current conversion efficiency (IPCE) was calculated using the equation

$$\text{IPCE} = i/F \cdot P, \quad (1)$$

where *i* is the photocurrent density, *F* is the Faraday constant (*F* = 96,485 C/mol), and *P* is the incident light intensity.

The electrochemical behavior of the layers was investigated by means of two methods: linear voltammetry and amperometry. Linear voltammetry provides information on the ability of the layers to generate the photocurrent upon illumination. In these tests the layers were irradiated with monochromatic light (UV – 365 nm) with periods of 5 s dark and 5 s light. The polarization curves were measured as the dependence of the current density on the imposed potential. A potential ramp from 400 to 1000 mV was applied to the working electrode with a scan rate of 10 mV/s. Amperometry is based on the photocurrent evaluation at a fixed potential (600 mV). The polarization curves were measured as the dependence of the current density on time. The 30-s dark interval was followed by 1-min interval of illumination. Each experiment ran for 4 min. The rate of electron/hole pair recombination can be estimated from the value of the measured open circuit potential. These experiments were again based on the combination of dark/light periods (total interval was 150 s) started in the dark for 30 s, the shutter was opened, and then the working electrode was irradiated for 60 s, after which 30 s in dark followed. The data were collected as the dependence of voltage on time.

### 2.5. Photocatalytic experiments

For testing the photoreactivities of the pristine and doped TiO<sub>2</sub> a glass reactor (cuvette, 30 × 50 × 10 mm) transmitting light with wavelengths longer than 290 nm was used. The UV irradiation was provided by a 400 W high-pressure mercury lamp (HQL 400 W; Osram, Munich, Germany) for 140 min. The distance between the lamp and the reactor was 10 cm, and the measured intensity of the UV radiation reaching the reactor was found to

be  $\sim 20 \text{ mW cm}^{-2}$ . The activities were quantified by the decoloration rate of Rhodamine B (RhB,  $\text{C}_{28}\text{H}_{31}\text{ClN}_2\text{O}_3$ ,  $V = 10 \text{ ml}$ ,  $c_0 = 10^{-4} \text{ mol l}^{-1}$ ) with absorbance at 553 nm measured by a UV/Vis spectrometer (Helios  $\gamma$ ; Thermo Electron Corporation; software Vision 32). The photocatalytic oxidation of Rhodamine B and also other dyes fitted the Langmuir–Hinshelwood kinetics model [50]. Since the initial RhB concentration was a millimolar solution, the equation can be simplified to an apparent first-order form [51] as

$$\ln \frac{c_0}{c} = k \cdot K \cdot t = k_{app} \cdot t, \quad (2)$$

where  $c_0$  is the initial RhB concentration,  $c$  is the RhB concentration in time  $t$ ,  $t$  is the illumination time,  $k$  is the reaction rate constant,  $K$  is the adsorption coefficient of RhB, and  $k_{app}$  is the apparent rate constant.

### 3. Results and discussion

#### 3.1. X-ray diffraction

Fig. 1 shows the XRD patterns of pristine and doped  $\text{TiO}_2$  thin layers. As can be seen only the anatase phase was identified. The average particle size was estimated by applying the Scherrer formula on the anatase diffraction peaks. It was revealed that introduction of the metal ions into  $\text{TiO}_2$  reduced the anatase grain size in all cases. The estimated grain size ( $d_p$ ) of naked  $\text{TiO}_2$  was 13.7 nm, whereas in the case of  $\text{Fe}/\text{TiO}_2$  it was found to be 9.7 nm. It is believed that the position of the dopants depends on the ionic size of the “foreign” metal. Once the ionic radius is smaller than  $\text{Ti}^{4+}$ , which is 0.69 Å, the ion likely enters the lattice by the substitution manner. Analogously, those ions larger than  $\text{Ti}^{4+}$  would be incorporated in the lattice as interstitials. According to this theory the  $\text{Fe}^{3+}$  ions should act as substitution dopants in the lattice of  $\text{TiO}_2$  [52]. This might be a reasonable explanation for the grain size reduction. However, a slight decrease of the anatase particle was observed also for the  $\text{Ag}/\text{TiO}_2$  and  $\text{Zr}/\text{TiO}_2$  with an ion radius of 1.26 and 0.84 Å, respectively.

#### 3.2. Raman spectroscopy

Raman spectroscopy was performed in order to obtain some additional information on the layers' crystallinity (Fig. 2). This phenomenon has already been noted previously [53]. The Raman spectra of pristine titania show only the typical features of nanocrystalline anatase. The anatase form displays the tetragonal structure and it belongs to the space group  $D_{19}^{4h}$  (I4/amd). With respect to

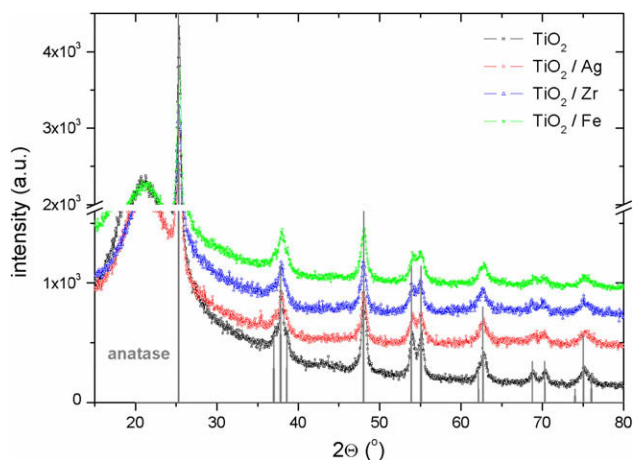


Fig. 1. X-ray diffraction patterns of bare  $\text{TiO}_2$  and doped titania samples.

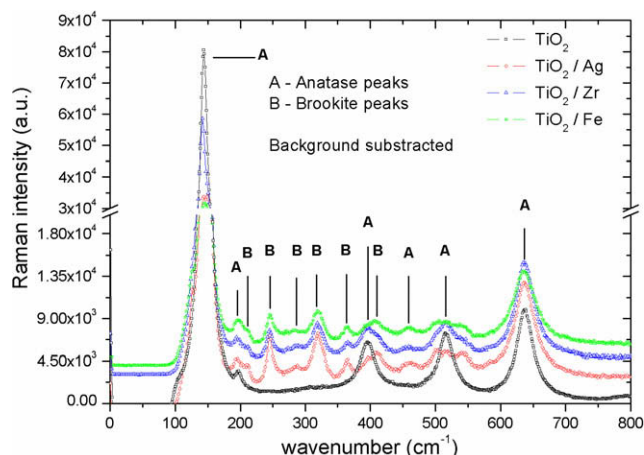


Fig. 2. Raman shifts of the prepared thin films.

the particular group, 10 optical modes can be identified—representing the structure:  $1A_{1g} + 1A_{2u} + 2B_{1g} + 1B_{2u} + 3E_g + 2E_u$ . The modes  $A_{2u}$  and  $E_u$  are active in the IR spectra and modes  $A_{1g}$ ,  $B_{1g}$ , and  $E_g$  in the Raman spectra. Only the first-order anatase Raman peaks at 638, 519, 513, 395, 196, and  $143 \text{ cm}^{-1}$  (highest intensity) are present in Raman spectra of pristine  $\text{TiO}_2$  [54]. This result correlates well with the X-ray data. However, the Raman spectroscopy showed that all the doped layers contained also a certain proportion of the brookite phase. This transformation was likely due to the dopants, which, as already noted, led to the suppression of the anatase particles. With the decrease of the grain size the total boundary energy of  $\text{TiO}_2$  layers increases. Simultaneously, the driving force for the brookite grain growth then increases and the anatase-to-brookite phase transformation is promoted [55]. The Raman lines of the brookite structure can be clearly distinguished in the spectra:  $A_{1g}$  ( $156, 190, 241, 405, 630 \text{ cm}^{-1}$ ),  $B_{1g}$  ( $314 \text{ cm}^{-1}$ ),  $B_{2g}$  ( $360, 395, 498, 585 \text{ cm}^{-1}$ ), and  $B_{3g}$  ( $449 \text{ cm}^{-1}$ ). The brookite form of  $\text{TiO}_2$  reveals the orthorhombic structure corresponding to the  $D_{2h}^{15}$  space group [56].

#### 3.3. XPS

The overall XPS spectrum taken from the silver-doped titania layer is shown in Fig. 3a. Moreover, Fig. 3 contains also detailed, highly resolved XPS spectra of Ag, Zr, Fe, Ti, and O atoms, respectively (Fig. 3b–f) recorded by analyzing the particular samples. The binding energies of Ag  $3d_{5/2}$  ( $367.3 \text{ eV}$ ), Zr  $3d_{5/2}$  ( $181.9 \text{ eV}$ ), and Fe  $2p_{3/2}$  ( $711 \text{ eV}$ ) and peaks can be assigned to  $\text{Ag}^0$ ,  $\text{Zr}^{4+}$ , and  $\text{Fe}^{3+}$ , respectively (Fig. 3b–d). The binding energy of Ag  $3d_{5/2}$  indicates that silver appears here in its metallic nature. Since the radius of  $\text{Ag}^+$  (1.26 Å) is much larger than that of  $\text{Ti}^{4+}$  (0.69 Å),  $\text{Ag}^+$  ions introduced by the sol–gel process would not enter the lattice of titania, but they remain collected at the surface of  $\text{TiO}_2$ . For the  $\text{Ag}^+$  ions spreading on the surface of  $\text{TiO}_2$ , under the action of heat, they would be reduced into  $\text{Ag}^0$  due to the high redox potential for the  $\text{Ag}^+$  ion. Also the Ag–O bonding is much weaker than Ti–O bonding (or Ag–Ag bonding) and Ag has a higher surface free energy than  $\text{TiO}_2$  [57,58]. Peaks for Ti  $2p_{3/2}$  and Ti  $2p_{1/2}$  for pure  $\text{TiO}_2$  films were observed at 459.1 and 464.8 eV, respectively. The peak separation was 5.7 eV, indicating the presence of  $\text{Ti}^{4+}$  ( $\text{TiO}_2$ ) in these films (Fig. 3e). The peak separation (5.7 eV) between Ti  $2p_{1/2}$  and Ti  $2p_{3/2}$  was retained after doping in all samples. The O 1s binding energy levels can be found as two peaks around 530 and 532 eV; the 530 eV peak is due to  $\text{O}^{2-}$  ions. The peak around 532 eV can be attributed to the surface hydroxyl groups or chemisorbed water molecules on titanium dioxide (Fig. 3f).

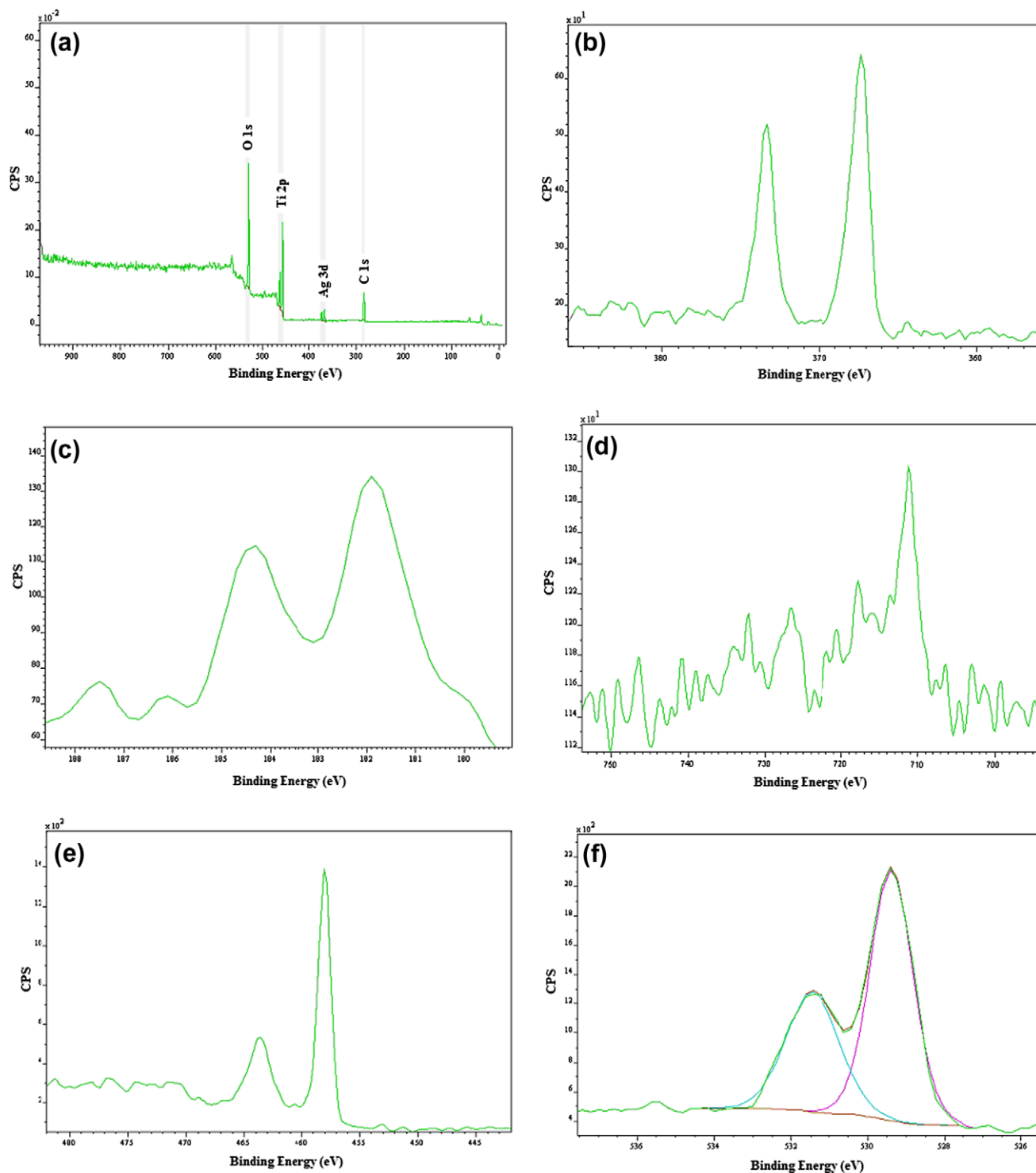


Fig. 3. XPS spectra of (a) silver-doped titania layer, highly resolved XPS spectra of Ag (b), Zr (c), Fe (d), Ti (e), and O (f).

### 3.4. Optical properties of the layers

In terms of the photo-induced catalytic and electrochemical processes the position of the absorption edge of the semiconductor working as the catalyst or the electrode is one of the more important parameters. Visible-ultraviolet absorption spectra of the pristine and doped  $\text{TiO}_2$  layers are shown in Fig. 4. Very often a shift in the band gap transitions toward longer wavelengths is observed for the doped layers. It is clearly demonstrated (Fig. 4) that the absorption edges are almost overlapped regardless of the presence

of the “foreign” atoms. Highly similar optical features of the layers are beneficial, because the studied system is thus less of one variable. The absorption onset was estimated to be  $\sim 370$  nm for all tested layers.

### 3.5. Morphology of layers

AFM images of the tested surfaces are displayed in Fig. 5. Besides a direct insight into the morphology of the films, the AFM method also provides an evaluation of the relative surface

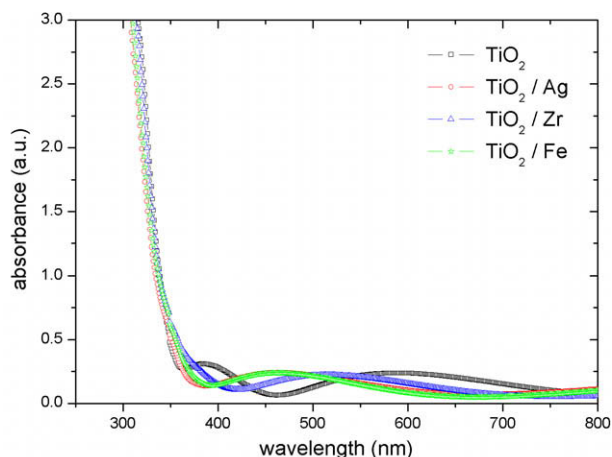


Fig. 4. UV-Vis absorption spectra of the samples.

roughness expressed as the rms value (summarized in Table 1).

Because of exactly the same preparation procedure the AFM pictures reflect directly the influence of the present dopant on the surface ordering. The smoothest surface was identified in the

**Table 1**

Basic physical parameters of the prepared layers.

Type of layer	$d_p^a$ (nm)	rms (nm)	The dopant content (at.%)	$k_{app} \times 10^3$ ( $\text{min}^{-1}$ )	IPCE <sup>b</sup>
TiO <sub>2</sub>	13.71	2.9	–	5.71	$1.95 \times 10^{-3}$
TiO <sub>2</sub> /Ag	11.79	4.45	1.17	10.1	$1.84 \times 10^{-3}$
TiO <sub>2</sub> /Zr	11.73	6.34	1.52	7.3	$1.13 \times 10^{-3}$
TiO <sub>2</sub> /Fe	9.7	3.13	0.35	6.2	$4.97 \times 10^{-4}$

<sup>a</sup>  $d_p$  – grain size.

<sup>b</sup> IPCE value at 175 s from amperometry measurements.

case of pristine TiO<sub>2</sub> with an average roughness of 2.9 nm. A slight increase of the roughness was observed for layers doped with Ag and Fe (4.45 and 3.13, respectively). As seen in Fig. 5, the lowest surface homogeneity embodied titania layers doped with Zr (rms 6.34 nm). However, all the layers can be referred to as smooth, free of defects, and with a high level of surface species ordering (here except TiO<sub>2</sub>/Zr).

SEM gives other interesting results (Fig. 6). While the SEM picture of the pristine titania layer reflects the results obtained by AFM (smooth surface, no defects, highly oriented species), some new information can be extracted from the SEM photographs of the remaining samples. Particularly it is the presence of the nucleating centers. Such centers initiate the crystal growth, especially in

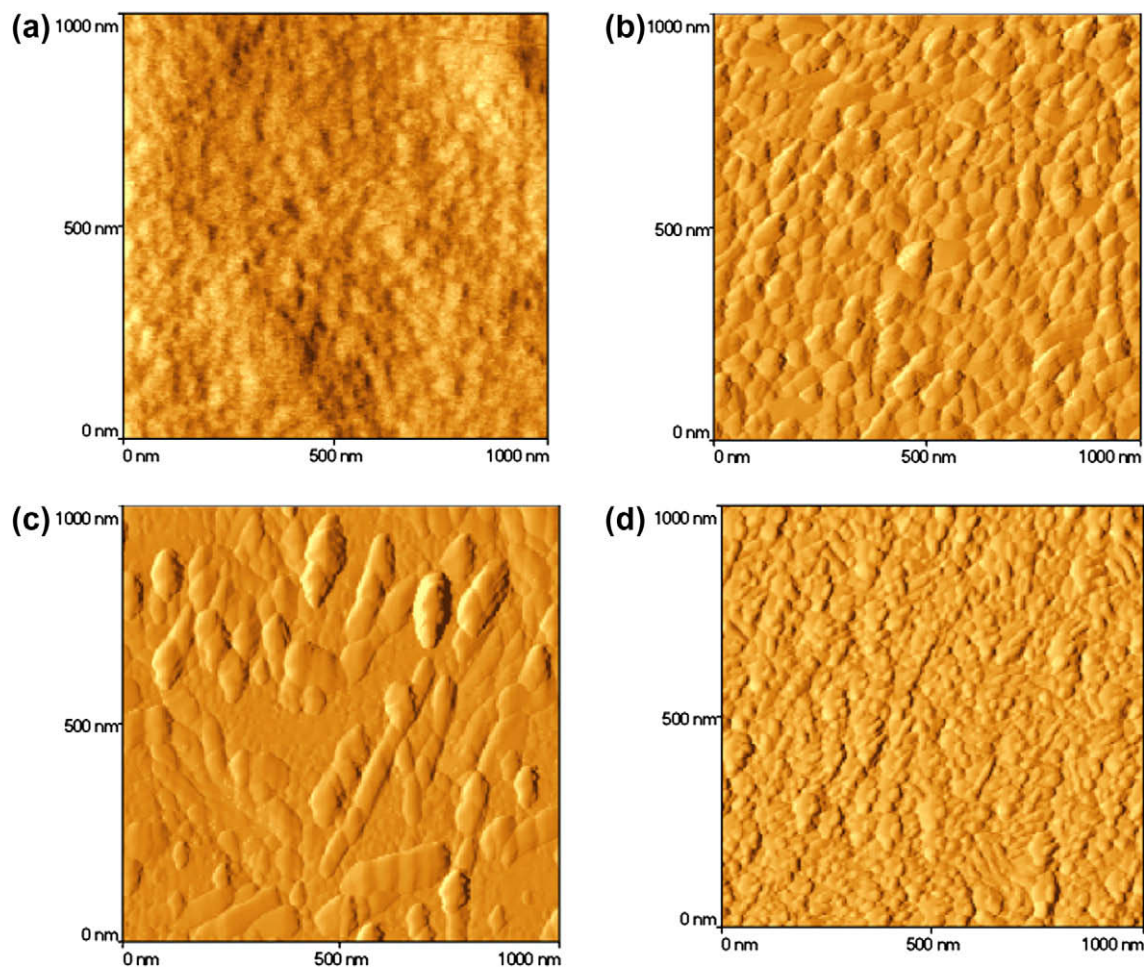


Fig. 5. AFM images of bare TiO<sub>2</sub> film (a), doped titania layers—Ag (b), Zr (c), and Fe (d).

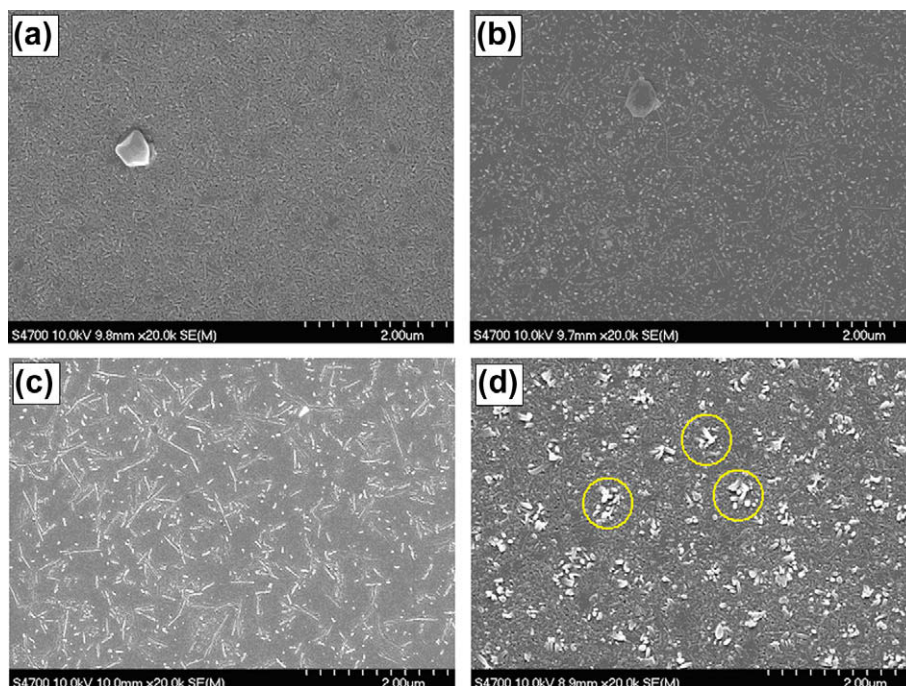


Fig. 6. SEM images of bare TiO<sub>2</sub> film (a), doped titania layers—Ag (b), Zr (c), and Fe (d).

their close neighborhood [59]. Obviously this phenomenon can be seen most clearly from the SEM picture of Fe-doped TiO<sub>2</sub> (Fig. 6d, circles).

The AFM data for the Zr/TiO<sub>2</sub> layers already revealed a capillary-like shape of the crystals aggregates. Such structure is more distinctly visualized by SEM (Fig. 6c). Regardless of the existence of the nucleating centers the SEM analysis did not reveal any extra defects.

### 3.6. Electrochemistry of layers

Polarization curves are shown in Fig. 7. The measurements were carried out at constant pH of 4.5 and at room temperature. Originally, this measurement is provided as the dependence of current density on the applied potential, in other words, the  $i$ - $V$  characteristic. However, the obtained current density values were, according to Eq. (1), recalculated to IPCE parameter. The polarization curves reflect the ability of the layers to generate the carriers (electrons and holes) on illumination with light of the appropriate wavelength. As a response, the electrons migrate through the layer toward the conducting back layer (ITO) whereas the holes promote oxidation reaction at the surface. Therefore, simply the so-called photocurrent flows.

The highest quantum yields, which also mean the highest photocurrents, were obtained for pristine TiO<sub>2</sub> and Zr/TiO<sub>2</sub>. The highest reached IPCE values are very similar in these cases, but the curves' trends are different. Relative slow growth of the photocurrent curve in the case of Zr/TiO<sub>2</sub> is apparently caused by electron traps created in the band gap due to the presence of the dopant. Besides the interior states of the band gap acting as the traps, the photocurrent value is significantly influenced by the light penetration depth (determines the amount of the generated carriers) and the layer porosity (determines the electrons ability to migrate). On the other hand, these parameters can be probably excluded, since the compared layers have the same thickness and are also structurally similar. As a result, the theory of electron trapping seems to be applicable. Further a significant decrease in IPCE

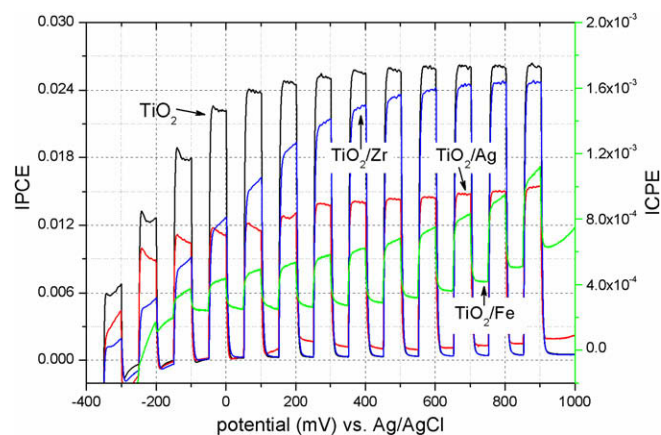


Fig. 7. Linear voltammetry responses.

is observed. While in the case of Ag/TiO<sub>2</sub> the IPCE is almost two times lower compared to pristine TiO<sub>2</sub>, it is practically negligible for Fe/TiO<sub>2</sub>. In order to make the IPCE data (Fe/TiO<sub>2</sub>) readable in the graph (Fig. 7), a second y-axis with a scale 15 times lower than the original one was added (right y-axis). Since only the presence of “foreign” atoms (here Fe) in titania causes the main difference among the tested layers, the electron trapping is apparently the only plausible explanation [60–62]. As the electron traps, variously ionized oxygen vacancies growing in a higher amount due to charge compensation are meant. Oxygen vacancies are created most readily in the case of Fe/TiO<sub>2</sub>, in which Fe<sup>3+</sup> ions are probably substitutionally bound. As a consequence the trapped electrons cannot reach the conducting back-contact—resulting in the low value of the photocurrents [63]. The occurring dark current is perhaps due to the continuous defilling of the traps, rather than due to the depolarization of the electrode.

The layers were further tested for their ability to produce a constant amount of carriers, which is sought to be independent of time (invariant photocurrents). For this purpose the time dependence of

photocurrent at a fixed potential of 0.6 V was recorded (amperometry measurements).

At first sight, it is obvious (as expected) that the results reflect the preceding discussion (Fig. 8). Nevertheless, it is worth noting the very sharp IPCE maximum (current peak) appearing immediately after the light is on. The peak is explained as an instantaneous electrons/holes separation [64]. Considering the previous discussion, the presence of the traps in the band gaps should reduce also the current peak height because only few electrons reach the back-contact. This assumption correlates well with the results. The higher the current peak, the higher the IPCE value (compare Figs. 7 and 8). To display the curve corresponding to the time response of Fe/TiO<sub>2</sub> another y-axis (right y-axis) was again used. No current peak can be observed in this case, which underlines the mentioned hypothesis. However, the overall photocurrent stability with time can be regarded as poor for all the layers as a significant decrease of the IPCE value is evident from the graph.

### 3.7. Photocatalytic activity

The photocatalytic activity of pure and doped titanium dioxide thin films was examined by the decomposition of Rhodamine B. The apparent rate constants of RhB ( $k_{app}$ ) obtained from the slopes (Fig. 9) are reported in Table 1. The TiO<sub>2</sub> films, pure and also doped, effectively decomposed the RhB and the rate constants were found between  $5.7 \times 10^{-3}$  and  $10.1 \times 10^{-3} \text{ min}^{-1}$ . For TiO<sub>2</sub> films doped with Ag, Zr, and Fe the rate constants were enhanced significantly. The best apparent degradation rate constant ( $10.1 \times 10^{-3} \text{ min}^{-1}$ ), which was almost two times higher than that of the pure TiO<sub>2</sub> film, was obtained on the Ag/TiO<sub>2</sub> photocatalyst. The photodecomposition rate could be enhanced because more charge carriers are available [27,42,60]. According to the principle of photocatalysis, in the Zr- and Ag-doped TiO<sub>2</sub> films, the metal can provide a shallow trap for the photo-generated electron, thus inhibiting recombination and extending the lifetime of the charge carriers (electrons and holes). However, some dopants can negatively affect the photoreactivity of TiO<sub>2</sub> by changing the number of active sites, the surface group type, or the acid–base properties. The occurrence of such negative effects mostly depends on the preparation procedure and the dopant concentration. The different behavior of various samples is also related to the solubility of the transition metal in the support, which depends on the ion radius and charge. In this study Fe was found to be the worst dopant. This can be caused by low diffusion length and Fe can also serve as a trap for the electrons produced under irradiation. Nevertheless, the photocatalytic activity of Fe/TiO<sub>2</sub> was still found to be greater than that of pristine TiO<sub>2</sub>.

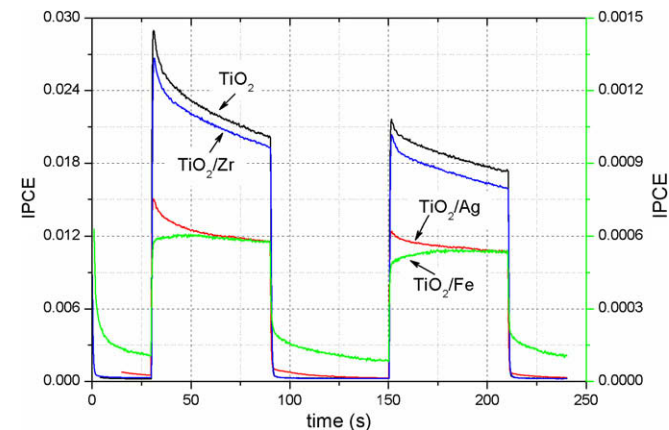


Fig. 8. Amperometry measurements.

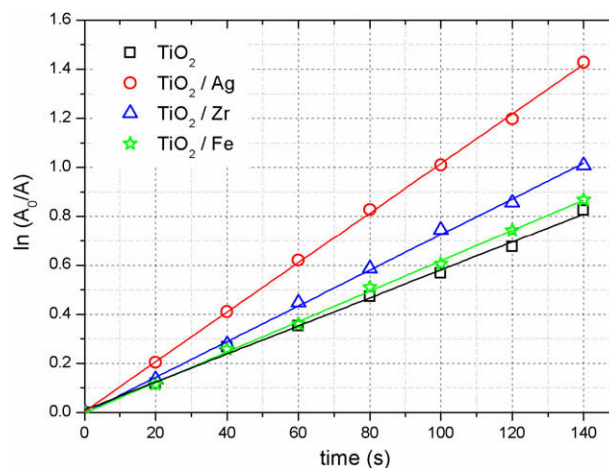


Fig. 9. Raw photocatalytic data of RhB decomposition on the layers.

Attention must be turned to the comparison between the photoelectrochemical and photocatalytic properties of the layers. There is an obvious and fundamental change in the photo response, although it should be consistent. It was established, in the Introduction, that the electron–hole pair recombination might be avoided by applying a voltage on the electrode coated by TiO<sub>2</sub>. It is seen in Fig. 7 that the highest photoelectrochemical response is found in the undoped types of layers, while these layers were determined to be the worst in terms of the photocatalytic activity. In other words, the pristine TiO<sub>2</sub> obviously suffers from a high rate of the electron–hole pair recombinations, which is reflected in its poor photocatalytic activity. However, according to the theory, as soon as the voltage is applied the electrons are swept toward the rear conducting contact of the support, and thus the carriers recombination is limited. This confirms the preceding assumption and as a result, the photoelectrochemical response is enhanced. On the other hand, the dopants in TiO<sub>2</sub> usually serve as electron traps aiding the electron–hole pair separation. This phenomenon could explain their better photocatalytic activity. It was shown that although the Fe/TiO<sub>2</sub> layers were electrochemically almost inactive (trapped electrons could not promote the photocurrent), they still revealed photocatalytic activity. However, the enhancement of the photocatalytic activity may possibly be attributed further to a certain synergic effect of the polycrystalline (anatase + brookite) nature of the layers [65] as well as to the higher specific area of the catalysts due to smaller grains [28] and higher surface roughness.

## 4. Conclusion

Pure and transition metal-doped TiO<sub>2</sub> thin films have been prepared via the sol–gel process. Only the anatase phase was found in the X-ray diffraction patterns recorded for undoped TiO<sub>2</sub>; however, in the case of transition metal-doped TiO<sub>2</sub> the brookite phase was also found. These results were confirmed by Raman spectroscopy. It can be concluded from the measurement of SEM and AFM that the pure TiO<sub>2</sub> thin film revealed a smooth surface and a slight increase of the surface roughness was observed for doped TiO<sub>2</sub> films. The degradation efficiency of the prepared films was examined by the decomposition rate of Rhodamine B. It has been found that the presence of metal dopants effectively increases the photocatalytic activity of TiO<sub>2</sub> thin films in the following order: Ag/TiO<sub>2</sub> > Zr/TiO<sub>2</sub> > Fe/TiO<sub>2</sub> > TiO<sub>2</sub>. The obtained polarization curves of the prepared films reflect the ability to generate the charge carriers. The highest quantum yields were determined for TiO<sub>2</sub> and Zr/TiO<sub>2</sub> thin films. Titania and transition-metal-doped titania thin

films produced by the sol–gel method revealed very interesting photocatalytic and opto-electrochemical properties and they might be considered as useful coatings for various applications (photocatalysis, sensors).

### Acknowledgments

The authors thank the Grant Agency of the Academy of Sciences of the Czech Republic, Projects KAN400720701 and KAN3013707 01, the Grant Agency of the Czech Republic (104/09/0694 and 202/08/1009), and the Ministry of Education of the Czech Republic, Project NanoPin No. 1M0577 for funding this research.

### References

- [1] T.M. Twesme, D.T. Tompkins, M.A. Anderson, T.W. Root, *Appl. Catal. B* 64 (2006) 153.
- [2] M. Abdullah, G.K.C. Low, R.W. Matthews, *J. Phys. Chem.* 94 (1990) 6820.
- [3] J.M. Coronado, M.E. Zorn, I. Tejedor-Tejedor, M.A. Anderson, *Appl. Catal. B* 43 (2003) 329.
- [4] R.T. Zehr, M.A. Henderson, *Surf. Sci.* 602 (2008) 2238.
- [5] I. Dolamic, T. Burgi, *J. Phys. Chem. B* 110 (2006) 14898.
- [6] N. Doucet, O. Zahraa, M. Bouchy, *Catal. Today* 122 (2007) 168.
- [7] S. Irmak, E. Kusvuran, O. Erbatur, *Appl. Catal. B* 54 (2004) 85.
- [8] C. Guillard, S. Horikoshi, N. Watanabe, H. Hidaka, P. Pichat, *J. Photochem. Photobiol. A* 149 (2002) 155.
- [9] K. Zakrzewska, *Vacuum* 74 (2004) 335.
- [10] G.K. Keima, M.J. Colgan, M.J. Brett, *Sol. Energy Mater. Sol. Cells* 85 (2005) 321.
- [11] O. Zywitki, T. Modes, H. Sahm, P. Frach, K. Goedicke, D. Glob, *Surf. Coat. Technol.* 180–181 (2004) 538.
- [12] P. Kluson, S. Kment, H. Bartkova, Z. Hubicka, in: *New Research on Thin Solid Films*, Nova Science, Hauppauge, NY, 2007.
- [13] Ch.-S. Kim, B.K. Moon, J.-H. Park, S.T. Chung, S.-M. Son, *J. Cryst. Growth* 254 (2003) 405.
- [14] S.-H. Lee, M. Kang, S.M. Cho, G.Y. Han, B.-W. Kim, K.J. Yoon, Ch.-H. Chung, *J. Photochem. Photobiol. A* 146 (2001) 121.
- [15] D. Byen, Y. Jin, B. Kim, *J. Hazard. Mater.* 73 (2000) 199.
- [16] J.P. Waters, D. Smyth-Boyle, K. Govender, A. Green, J. Durrant, P. O'Brien, *Chem. Vap. Deposition* 11 (2005) 254.
- [17] Z. Juan, B. Li, J. Zhang, C. Xu, *J. Sol-Gel Sci. Technol.* 39 (2006) 249.
- [18] C. Su, B.-Y. Hong, C.-M. Tseng, *Catal. Today* 96 (2004) 119.
- [19] E.I. Ko, in: *Handbook of Heterogeneous Catalysis*, Wiley-VCH, Weinheim, Germany, 1997.
- [20] T. Noguchi, A. Fujishima, *Environ. Sci. Technol.* 32 (1998) 3831.
- [21] P. Kluson, H. Luskova, T. Cajthaml, O. Solcova, *Thin Solid Films* 495 (2006) 18.
- [22] P. Kluson, P. Kacer, T. Cajthaml, M. Kalaji, *Chem. Biochem. Eng. Q.* 17 (2003) 183.
- [23] C. Galindo, P. Jacques, A. Kalt, *J. Photochem. Photobiol. A* 130 (2000) 35.
- [24] N. Daneshvar, D. Salari, A.R. Khataee, *J. Photochem. Photobiol. A* 157 (2003) 111.
- [25] J. Bandara, J.A. Milczarski, J. Kiwi, *Langmuir* 15 (1999) 7680.
- [26] S. Kim, S.J. Hwang, W. Choi, *J. Phys. Chem. B* 109 (2005) 24260.
- [27] J. Chen, M. Yao, X. Wang, *J. Nanopart. Res.* 10 (2008) 163.
- [28] Z. Ambrus, N. Balázs, T. Alapi, G. Wittmann, P. Sipos, A. Dombi, K. Mogyorósi, *Appl. Catal. B* 81 (2008) 27.
- [29] M. Subramanian, S. Vijayalakshmi, S. Venkataraj, R. Jayavel, *Thin Solid Films* 516 (2008) 3776.
- [30] T.L.M. Martínez, C. Montes de Correa, J.A. Odriozola, M.A. Centeno, *J. Mol. Catal. A* 253 (2006) 252.
- [31] M.M. Mohamed, I. Otoman, R.M. Mohamed, *J. Photochem. Photobiol. A* 191 (2007) 153.
- [32] Ch.-G. Wu, Ch.-Ch. Chao, F.-T. Kuo, *Catal. Today* 97 (2004) 103.
- [33] I. Tsuyumoto, K. Nawa, *J. Mater. Sci.* 43 (2008) 985.
- [34] Z.H. Li, H. Dong, Y.F. Zhang, *J. Phys. Chem. C* 112 (2008) 16046.
- [35] Y.K. Du, Y.Q. Gan, P. Yang, F. Zhao, N.P. Hua, L. Juany, *Thin Solid Films* 491 (2005) 133.
- [36] C. Garzella, E. Comini, E. Bontempi, L.E. Depero, C. Frigari, G. Sterveglieri, *Sens. Actuators B* 83 (2002) 230.
- [37] Y. Wang, Y. Hao, H. Cheby, J. Ma, B. Xu, W. Li, S. Cai, *J. Mater. Sci.* 34 (1999) 2773.
- [38] N. Venkatachalam, M. Palanichamy, B. Arabindoo, V. Murugesan, *J. Mol. Catal. A* 266 (2007) 158.
- [39] P.E. Lippens, A.V. Chadwick, A. Weibel, R. Bouchet, P. Knauth, *J. Phys. Chem. C* 112 (2008) 43.
- [40] I.M. Arabatzis, T. Stergiopoulos, M.C. Bernard, D. Labou, S.G. Neophytides, P. Falaras, *Appl. Catal. B* 42 (2003) 187.
- [41] D.B. Hamal, K.J. Klabunde, *J. Colloid Interface Sci.* 311 (2007) 514.
- [42] A. Di Paola, G. Marci, L. Palmisano, M. Schiavello, K. Upsali, S. Ikeda, B. Ohtani, *J. Phys. Chem. B* 106 (2002) 637.
- [43] Ch. He, Y. Yu, X. Hu, A. Larbot, *Appl. Surf. Sci.* 200 (2002) 239.
- [44] S.T. Martin, C.L. Kortison, M.R. Hoffmann, *J. Phys. Chem.* 98 (1994) 13695.
- [45] J. Krysa, M. Keppert, G. Waldner, *Electrochim. Acta* 50 (2005) 5255.
- [46] G. Waldner, J. Krysa, *Electrochim. Acta* 50 (2005) 4498.
- [47] S. Kment, P. Kluson, V. Stranak, P. Virostko, J. Krysa, M. Cada, J. Pracharova, M. Kohout, M. Morozova, P. Adamek, Z. Hubicka, *Electrochim. Acta* 54 (2009) 3352.
- [48] S. Kment, P. Kluson, Z. Hubicka, J. Krysa, M. Cada, I. Gregora, A. Deyneka, Z. Remes, H. Zabova, L. Jastrabik, *Electrochim. Acta* 55 (2010) 1548.
- [49] H. Zabova, V. Cirkva, *J. Chem. Technol. Biotechnol.* 84 (2009) 1624.
- [50] S. Qourzal, M. Tamini, A. Assabbane, A. Bouamrane, A. Nounah, L. Laanab, *J. Appl. Sci.* 6 (2006) 1553.
- [51] Y. Ao, J. Xu, D. Fu, C. Yuan, *Appl. Surf. Sci.* 255 (2008) 3137.
- [52] C.E. Rodriguez-Torres, A.F. Cabrera, L.A. Errico, C. Adan, F.G. Requejo, M. Weismann, S.J. Stewart, *J. Phys. Condens. Mater.* 20 (2008) 135210.
- [53] J.H. Pan, W.I. Lee, *Chem. Mater.* 18 (2006) 847.
- [54] Y. Hu, H.-L. Tsai, C.-L. Huang, *Mater. Sci. Eng. A* 344 (2003) 209.
- [55] T. Ohsaka, F. Izumi, Y. Fujiki, *J. Raman Spectrosc.* 7 (1978) 321.
- [56] G.A. Tompsett, G.A. Bowmaker, R.P. Cooney, J.B. Metson, K.A. Rodgers, J.M. Seakins, *J. Raman Spectrosc.* 26 (1995) 57.
- [57] H.E. Chao, Y.U. Yun, H.U. Xingfang, A. Larbot, *J. Eur. Ceram. Soc.* 23 (2003) 1457.
- [58] Y. Ao, J. Xu, D. Fu, C. Yuan, *J. Phys. Chem. Solids* 69 (2008) 2660.
- [59] Ch.Ch. Chang, J.Y. Chen, T.L. Hsu, Ch.K. Liu, Ch.Ch. Chan, *Thin Solid Films* 516 (2008) 1743.
- [60] W. Choi, A. Termin, M. Hoffmann, *J. Phys. Chem.* 98 (1994) 13669.
- [61] M.I. Litter, J.A. Navio, *J. Photochem. Photobiol. A* 98 (1996) 171.
- [62] N. Serpone, D. Lawless, *Langmuir* 10 (1994) 643.
- [63] X. Zhang, L. Lei, *Mater. Lett.* 62 (2008) 895.
- [64] J.A. Byrne, Brian R. Eggins, *J. Electroanal. Chem.* 457 (1998) 61.
- [65] T. Ozawa, M. Iwasaki, H. Tada, T. Akita, K. Tanaka, S. Ito, *J. Colloid Interface Sci.* 281 (2005) 510.